

Measurement of transverse single-spin asymmetries for dijet production in polarized proton-proton collisions at $\sqrt{s} = 200$ GeV

(STAR Collaboration)

(Dated: February 6, 2024)

We report a new measurement of transverse single-spin asymmetries for dijet production in collisions of polarized protons at $\sqrt{s} = 200$ GeV. Correlations between the proton spin and the transverse momenta of its partons, each perpendicular to the proton momentum direction, are probed at high $Q^2 \approx 160$ GeV². The associated Siverson observable $\langle k_T \rangle$, the average parton transverse momentum, is extracted using simple kinematics. Nonzero Siverson effects are observed for the first time in dijets from proton-proton collisions, but only when the jets are sorted by their net charge, which enhances the u - or d -quark contributions to separate data samples. This also enables a simple kinematic approach for determination of the individual partonic contributions to the observed asymmetries.

Our understanding of the three-dimensional structure of the nucleon has progressed significantly in the past decades [1, 2] and will be further advanced at the future Electron-Ion Collider [3]. In momentum space, nucleon structure is typically expressed via transverse-momentum-dependent parton distribution functions (TMD PDFs) with explicit dependence on the intrinsic partonic transverse momentum (\vec{k}_T). One TMD PDF of particular interest is the spin-dependent Siverson function [4] f_{1T}^\perp which characterizes a scalar triple-vector correlation for an unpolarized parton and its transversely polarized parent proton: $(\vec{k}_T \times \vec{S}) \cdot \vec{P}$, where \vec{k}_T , \vec{S} and \vec{P} are the parton transverse momentum, proton spin and proton momentum, respectively. In hard scattering of transversely polarized protons, this correlation leads to a left-right asymmetry in the azimuthal distribution of produced particles. The Siverson effect was originally introduced [4] to explain the large transverse single-spin asymmetries (TSSA) observed in inclusive pion production, whose persistence to high transverse momenta p_T appeared contrary to QCD expectations [5], with recent extensive experimental confirmation [6]. Currently, in addition to the TMD PDF and fragmentation function (FF) framework that has expanded to describe the growing number of true TMD phenomena, a collinear formalism involving twist-3 distributions (quark-gluon-quark correlations) is being developed and is more applicable for describing single hadron TSSA effects. The Siverson function and its twist-3 analog, the Efremov-Teryaev-Qiu-Sterman (ETQS) distribution [7, 8], are related quantitatively [9], providing additional constraints and insight.

Experimental evidence for the Siverson effect was first observed [10] in semi-inclusive deep inelastic scattering (SIDIS) [11–15]. Fits to these data show opposite signs and similar scale for the u - and d -quark Siverson functions [16–25], with sea quarks compatible with zero. Valence quarks nearly saturate the Burkardt sum rule [26], leaving little room for gluon Siverson contributions. Building on an unpolarized TMD foundation [27], there is considerable recent interest in also combining TMD data from SIDIS, e^+e^- annihilation and pp scattering to arrive at a unified picture including effects of the Siverson function [24, 25, 28–30]. While there is, as yet, no formal connection between Siverson and orbital angular momen-

tum (OAM), the latter is a prerequisite [31] for the Siverson effect. These and other studies based on Siverson-related distributions [20] point to an emerging nucleon 3-D structure and further understanding of a possible contribution of OAM to the nucleon spin.

A distinctive feature of the Siverson function is its nonuniversality. QCD gauge invariance requires the Siverson function to be process dependent, a manifestation of the underlying color dynamics, resulting in opposite signs for the Siverson asymmetries in SIDIS and the Drell-Yan process [32]. Investigations are ongoing to confirm this predicted sign change using W^\pm/Z^0 boson production [33], with only rather qualitative support so far observed [29, 34, 35].

Dijet production in transversely polarized proton-proton collisions offers a means to directly probe the underlying spin-dependent partonic \vec{k}_T that characterizes the Siverson effect, via the opening-angle kinematic tilt that reverses under spin-flip of the proton beam [36]. Formally, the average $\langle k_T \rangle$ one extracts, samples $f_{1T}^{\perp(1)q}(x)$, the first transverse moment of the Siverson function [37], over the kinematic x -range of the measurement. The results can be related to calculation through detailed theoretical evaluation of dijet production. The dijet channel in pp collisions avoids spin-correlated fragmentation contributions, and at STAR investigates a higher Q^2 scale ($\gtrsim 160$ GeV²). While it involves contributions from gauge links associated with color in both the initial (as in Drell-Yan) and final (as in SIDIS) states [38], these measurements may serve to constrain uncertainties associated with the overall process dynamics.

An early analysis from STAR at the Relativistic Heavy Ion Collider (RHIC) found Siverson asymmetries consistent with zero in dijet production, mainly due to the cancellation between the u and d quarks, as well as limited statistics [39]. Deciphering any back-to-back dijet results in a theoretical framework faces challenges from TMD factorization breaking [40, 41] and resummation of large logarithmic terms. New Siverson dijet measurements may enable better insights and there are recent theoretical approaches spurred by such interest [42, 43]. We revisit the Siverson dijet measurement at STAR with a jet-charge tagging method to separate the u and d contributions, together with significantly improved statistics

from a larger data set. Increased precision arises from inclusion of charged particle tracking in jet reconstruction.

In this analysis, we use 200 GeV transversely polarized pp data collected in 2012 and 2015 at STAR, corresponding to an integrated luminosity of 22 pb^{-1} and 52 pb^{-1} , respectively. The involved subsystems of the STAR detector [44] are the Time Projection Chamber (TPC) [45], providing charged particle tracking for pseudorapidity $|\eta^{detector}| \leq 1.3$, and the Electromagnetic Calorimeter (EMC), measuring the energy of electrons and photons while providing jet triggering in the barrel $-1 < \eta^{detector} < 1$ (BEMC [46]) and endcap $1.1 < \eta^{detector} < 2$ (EEMC [47]) regions with full azimuthal (ϕ) coverage. The polarization for the $+z$ (direction at STAR) and $-z$ circulating beams is measured using Coulomb-nuclear interference proton-carbon polarimeters, calibrated with a polarized hydrogen gas-jet target. The average beam polarizations are 56% (2012) and 57% (2015), both with a relative scale uncertainty of 3.2% [48].

The data are recorded using an EMC jet-patch trigger with two levels of transverse energy (E_T) threshold in a $\Delta\eta \times \Delta\phi = 1 \times 1$ (radians) region: 5.4 GeV (JP1) and 7.3 GeV (JP2). Jets are reconstructed using the *Anti- k_T* [49] algorithm with $R = \sqrt{\Delta\phi^2 + \Delta\eta^2} = 0.6$, employed with standard STAR selection criteria on the TPC tracks, EMC towers and proto-jet quantities [50]. To ensure the quality of the dijets, we select events with exactly two jets, one having $p_T > 6 \text{ GeV}/c$ and the other $p_T > 4 \text{ GeV}/c$, at an opening angle $\Delta\phi > 120^\circ$. Both jets are required to originate from a single vertex with $|Z_{vertex}| < 90 \text{ cm}$, and orientation within $-0.8 < \eta < 1.8$ and $-0.7 < \eta^{detector} < 1.7$. In order to avoid false triggering effects, a trigger simulator is applied, which requires the matching of offline reconstructed jets with triggered jet patches. The resulting number of events is ~ 33 times more than that available in an earlier study [39].

The observable in this analysis relies on a precise knowledge of the jet direction (as compared to the magnitude of its momentum) and is the same as used previously [39], namely, the *signed dijet opening angle* (ζ) [36]. It is defined as $\zeta = |\Delta\phi|$ if $\cos(\phi_b) < 0$ and $\zeta = 360^\circ - |\Delta\phi|$ if $\cos(\phi_b) > 0$, where ϕ_b is the azimuthal angle of the bisector ray, which reverses direction when the beam polarization direction is flipped. The sensitivity of ζ to transverse spin effects is not azimuthally even. It is maximized when the two jets are parallel to the beam spin orientation, and modulated by $|\cos(\phi_b)|$, is effectively zero when the two jets are perpendicular to the spin orientation.

For our jet- p_T range, ζ is directly sensitive [36, 39] to \vec{k}_T and embodies a tight linear dependency. This correlation enables a conversion from the ζ asymmetries to Sivers (k_T), discussed further below. Our method to extract an asymmetry for the spin-dependent dijet response differs from a traditional single-spin analyzing power A_N . The asymmetry is calculated as the difference of ζ centroids ($\langle\zeta\rangle$) between the spin-up and spin-down states:

$$\Delta\langle\zeta\rangle = \frac{\langle\zeta\rangle^+ - \langle\zeta\rangle^-}{P}, \quad (1)$$

where $\langle\zeta\rangle^{+/-}$ is the centroid of the Gaussian-like [39] ζ distribution in the spin-up/spin-down state, and P is the beam polarization. Equation 1 has the advantage of avoiding several systematic uncertainties, such as relative luminosity, asymmetric detector azimuthal acceptance and similar potential contributions. $\langle\zeta\rangle$ is extracted by fitting the ζ distribution $N(\zeta)$ over a selected range with a three-Gaussian function capturing its salient features:

$$N(\zeta) = p_0 \cdot e^{-\frac{(\zeta-p_1)^2}{2p_2^2}} + p_3 \cdot e^{-\frac{(\zeta-p_1)^2}{2p_4^2}} + p_5 \cdot e^{-\frac{(\zeta-p_1)^2}{2p_6^2}}, \quad (2)$$

where all the Gaussian components share the same peak position p_1 , taken as $\langle\zeta\rangle$. The values of the centroid differences $\Delta\langle\zeta\rangle$ subsequently extracted are largely insensitive to variation of this empirically driven function shape [51]. Two fitting steps are performed: 1) spin-up and spin-down distributions, scaled to the same integral, are combined and fit to determine the individual Gaussian parameters; 2) spin-up and spin-down ζ distributions are separately fit with Eq. 2, during which only p_1 is allowed to vary, making the final fit results more sensitive to p_1 and improving accuracy. The broad ζ distribution, driven mainly by parton-level multi-GeV intrinsic k_T and initial-state radiation effects [52], nearly fills the analysed back-to-back dijet ζ range of $180 \pm 60^\circ$; our fit range of $180 \pm 50^\circ$ allows some room for systematic study.

The resulting $\Delta\langle\zeta\rangle$ vs. ϕ_b values are mapped to a range $[0^\circ, 90^\circ]$ with respect to the transverse spin direction and six bins fit with a cosine function, whose amplitude quantifies the measured asymmetry. The $\Delta\langle\zeta\rangle$ asymmetry is extracted separately in each of four ‘‘jet charge’’ bins within the subsets of JP triggers and 2012, 2015 data.

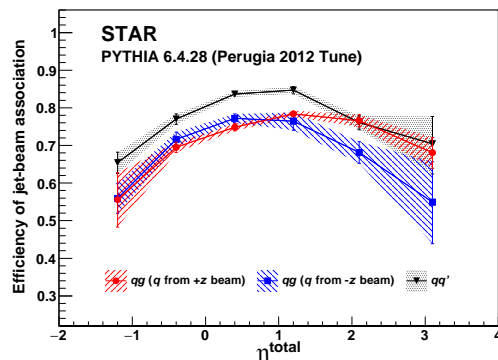


FIG. 1. Efficiency for associating beam and jet correctly in the embedding sample vs. η^{total} , the summed dijet η .

To avoid possible u - d cancellation, we divide the data into multiple kinematic regions in the analysis, each with a variant parton composition. The initial selection is based on the ‘‘tagging’’ of a jet, which needs first to be associated with the polarized beam. The more forward of the two jets (largest detector $|\eta|$) is assumed to be likely coming from the scattered parton originating from the beam pointing into the same hemisphere. For instance, in a dijet event with $\eta_1 > \eta_2$, jet_1 is associated with the $+z$ beam and jet_2 with the $-z$ beam. Performance of the beam-jet association is studied with simulation, developed based on Pythia 6.4.28 [53] (Perugia 2012

tune [52, 54]) and GEANT 3 [55], and embedded into randomly selected bunch crossings from data to mimic real beam background, pileup and detector inefficiencies. The Pythia energy scaling parameter PARP(90) is tuned down (0.240 to 0.213), improving agreement with inclusive pion production data at low p_T . Simulation reveals that the resulting association efficiency for qg and qq' subprocesses averages about 70%-75% (Fig. 1). This ensures good performance of jet tagging for the u and d quarks in the next step. (Note: for identical partons, gg and qq , the association is ambiguous).

During hadronization, the u quarks and d quarks produce relatively more positively charged and negatively charged particles, respectively. This feature can be quantified by jet charge (Q) [56] to help in tagging jets:

$$Q = \sum_{|p^{track}| > 0.8 \text{ GeV}/c} \frac{|p^{track}|}{|p^{jet}|} \cdot q^{track}, \quad (3)$$

where q^{track} represents the electric charge of each track. To reduce the influence from underlying events, only tracks with $|p| > 0.8 \text{ GeV}/c$ are selected in the calculation. The distributions of Q for different scattered partons are plotted using the embedding sample (Fig. 2), for which the effect of beam-jet association has also been folded in. Based on these plots, each data sample is divided into four “jet-charge” bins:

- + tagging: $Q \geq 0.25$, enhancing the fraction of u
- 0^+ tagging: $0 \leq Q < 0.25$, less enhancement of u
- 0^- tagging: $-0.25 < Q < 0$, less enhancement of d
- - tagging: $Q \leq -0.25$, enhancing the fraction of d

The four binned regions are expected to show different $\Delta\langle\zeta\rangle$ asymmetries in the presence of opposite signs of the Sivvers function for the u and d quarks.

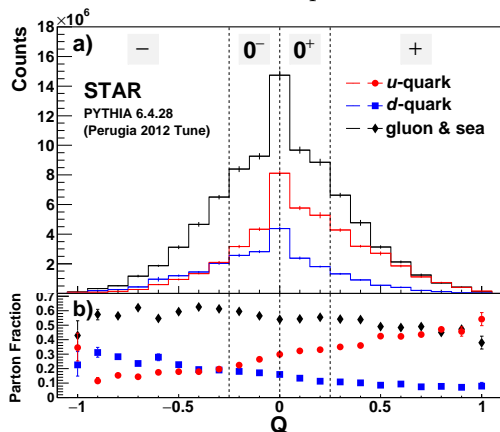


FIG. 2. The a) distribution of Q and b) respective parton fraction from the embedded simulation. The tagging divides the data sample into 4 bins (separated by the dashed lines).

Because the parton fraction is dependent on x , we further divide the full data set into η^{total} bins ($\eta^{total} = \eta_1 + \eta_2 \propto \log(x_1/x_2)$) [39]. We also combine the separate $+z$ and $-z$ polarized beam results, by transforming (rotation around the y -axis) the $-z$ beam $\Delta\langle\zeta\rangle$ asymmetries

into the $+z$ beam direction. The resulting $\Delta\langle\zeta\rangle$ asymmetries, now over an extended η^{total} range, for the four charge-tagged bins are shown in Fig. 3 a). We observe a $\sim 3.1\sigma$ separation between the averaged asymmetries in the $+$ tagging and the $-$ tagging. A correlation between $\Delta\langle\zeta\rangle$ and Q is also manifest, as the asymmetry shifts from negative to positive with the increment of Q (less d and more u). This is strong evidence that the Sivvers $\langle k_T \rangle$ effect for u and d are opposite, as indicated in SIDIS measurements [11–13] in a different type of analysis.

Our observed $\Delta\langle\zeta\rangle$ asymmetries are validated through several crosschecks. A null test made by calculating the asymmetry in the direction orthogonal to the expected Sivvers \vec{k}_T finds all the charge-tagged results consistent with zero, ruling out the possibility of major spin-dependent systematic effects. In the separated $+z$ beam and $-z$ beam measurements, we see overall consistency in sign and magnitude for the asymmetries within the same η^{total} bins and the same charge-tagged bins. Similar consistencies are also observed for the results using only 2012 or 2015 data. These and other studies show a statistical consistency in the measured asymmetries, indicating the systematic uncertainty is well under control.

In dijet events, the opening angle is closely tied to the p_T imbalance. This allows extraction of $\langle k_T \rangle$ results by correlating detector level $\Delta\langle\zeta\rangle$ and parton level $\langle k_T \rangle$, notably independent of intrinsic k_T characterization as verified by a dedicated simulation. To do the conversion, we first correct the jet p_T back to its parton level, based on machine learning using the embedded simulation sample. We adopt the same algorithm, variables and training configuration as in a previous analysis [50], but now targeted toward parton p_T instead of particle jet p_T . The weights from the training are applied to the jets in the real data to determine the actual p_T distribution. Next, the $\Delta\langle\zeta\rangle$ - $\langle k_T \rangle$ correlation is constructed using kinematics alone. We independently add two opposite constant $\langle k_T \rangle$ vectors, $(\langle k_T \rangle, 0, 0)$ and $(-\langle k_T \rangle, 0, 0)$, to the corrected events to mimic dijet tilts in nominal “spin-up” and “spin-down” states, respectively. A $\Delta\langle\zeta\rangle$ asymmetry at parton level is extracted following the above analysis procedure; the results are used at detector level with a systematic described further below. By assigning 5 different $\langle k_T \rangle$ values in the range 1-20 MeV/ c to the added vectors, an experimentally determined linear relation between $\Delta\langle\zeta\rangle$ and $\langle k_T \rangle$ is observed individually for each η^{total} bin, which can be well fit with a slope: $\Delta\langle\zeta\rangle = slope \cdot \langle k_T \rangle$. Due to p_T differences in η^{total} bins, the slope ranges from $9.26^\circ \cdot c/\text{GeV}$ in the mid-rapidity region to $9.97^\circ \cdot c/\text{GeV}$ in the more forward region.

The $\Delta\langle\zeta\rangle$ results are converted to $\langle k_T \rangle$ results, Fig. 3 b), by applying the reverse of the above calculated slope, $\langle k_T \rangle = \Delta\langle\zeta\rangle / slope$. The average $\langle k_T \rangle$ is found to be $3.2 \pm 1.9 \text{ MeV}/c$ for the $+$ tagging bin, and $-5.9 \pm 2.2 \text{ MeV}/c$ for the $-$ tagging bin. The untagged asymmetry, $-0.4 \pm 0.9 \text{ MeV}/c$, obtained from the error-weighted mean of the four charge-tagged bins, is consistent with zero. We observe a $\sim 2\sigma$ level linear η^{total} -dependency in the $+$ tag-

ging $\langle k_T \rangle$ results. This appears to be mainly attributed to the x -dependency of the parton fractions.

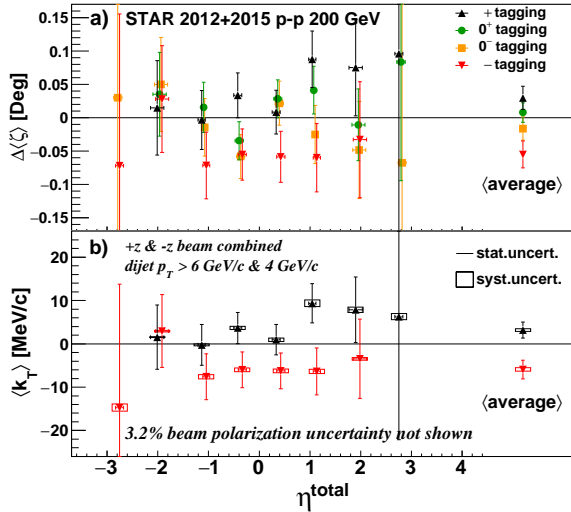


FIG. 3. The a) $\Delta\langle\zeta\rangle$ values and b) converted $\langle k_T \rangle$ plotted as a function of η^{total} . Rightmost points represent the average over the η^{total} bins. Individual 0^+ and 0^- points are suppressed in the lower panel to better view the $\langle k_T \rangle$ signal and systematic errors (dominated by fitting range contributions). Plotted points are offset in η^{total} and outsize values omitted for clarity.

The tagged $\langle k_T \rangle$ results provide sufficient constraints to solve for the $\langle k_T \rangle$ of individual partons once we learn the parton fractions in each charge-tagged bin, which can be estimated from simulation. A caveat here is that our inversion method is not intended to be theoretically rigorous, but assumes simple $2 \rightarrow 2$ scattering kinematics in our simulation sample, guiding the analysis and setting the scale of the Sivers $\langle k_T \rangle$ for individual partons. Combining the gluon and sea quark contributions, there are four constraints from charge tagging vs. three unknown variables: $\langle k_T^u \rangle$, $\langle k_T^d \rangle$ and $\langle k_T^{g+sea} \rangle$. To increase the stability of the inversion process, data from adjacent bins in η^{total} are combined, leading to the eight constraints:

$$f_{i,j}^u \langle k_T^u \rangle + f_{i,j}^d \langle k_T^d \rangle + f_{i,j}^{g+sea} \langle k_T^{g+sea} \rangle = \langle k_T \rangle_{i,j}, \quad (4)$$

where f represents the parton fraction from simulation [51], the right-hand side $\langle k_T \rangle$ is the tagged measurement in data, i runs over all the charge tagging bins, and j runs over the two adjacent η^{total} bins. The over-constrained system is solved through Moore-Penrose inversion yielding values for the individual parton $\langle k_T \rangle$, displayed in Fig. 4 and discussed further below.

The systematic uncertainty of the parton $\langle k_T \rangle$ has major contributions from two sources: the fitting range of ζ and the more dominant error associated with the estimation of parton fractions. The uncertainty associated with a choice of fit range is estimated by varying the range from $180 \pm 40^\circ$ to $180 \pm 60^\circ$, extracting $\langle \zeta \rangle$ for each trial, and calculating the average absolute deviation from the nominal fit range at $180 \pm 50^\circ$, separately in each η^{total} bin. The scale of the fit range uncertainty is less than 15% in the +tagging/-tagging as indicated in Fig. 3

b). The default matrix inversion process is then used to convert the uncertainty for the tagged asymmetries to that for individual partons. Separately, parton fractions are estimated with leading-order PYTHIA simulations, which come with their own set of systematic uncertainties. The largest contributing factors to the uncertainty are PDF and initial/final state radiation (ISR/FSR), as well as the statistics of the simulation sample. Different PDF sets directly cause discrepancies in the fraction of partons. The amount of ISR/FSR particularly affects event selection in the low p_T region, which leads to uncertainties in the parton fractions. These uncertainties due to PDF and ISR/FSR are estimated by varying respective PYTHIA tunes, comparing to the default tune (370) and quoting the average absolute difference. The statistical uncertainties of parton fractions are about the same level as the PDF and ISR/FSR uncertainties, and are added in quadrature to the total systematics. These total uncertainties vary with parton purity in the various charge bins and as a function of $-3.6 < \eta^{total} < 3.6$, ranging from 18 to 7-12% for u and d , and 3-21% for $g + sea$. Aside from fit range and parton fractions, there is a systematic associated with the parton level to detector level $\Delta\zeta$ mapping. Since $\Delta\zeta$ vs. $\langle k_T \rangle$ is observed to be linear, effects from broadening are small. A comparison of detector and parton level $\Delta\langle\zeta\rangle$ for a wide range of simulated $\langle k_T \rangle$, gives an estimated uncertainty of $\sim 5.6\%$, due largely to differences in average momentum for the various JP and run conditions considered.

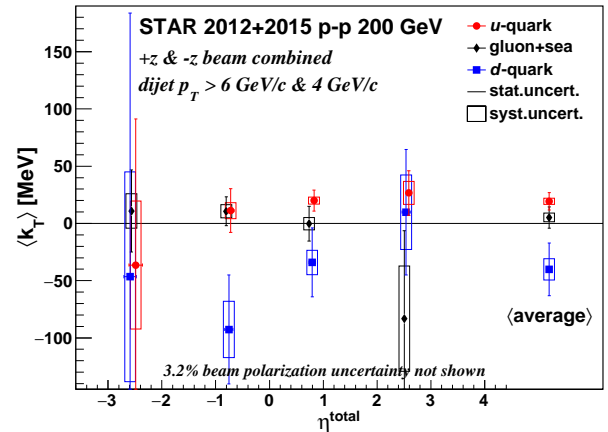


FIG. 4. The $\langle k_T \rangle$ for individual partons, inverted using parton fractions from simulation and tagged $\langle k_T \rangle$, plotted as a function of η^{total} , with rightmost points the η^{total} average. Plotted points are offset in η^{total} for clarity, and systematic uncertainties in η^{total} are set nonzero to improve visibility.

The inverted results and average over all the η^{total} bins are shown in Fig. 4 and summarized here. The average $\langle k_T^u \rangle$ is estimated to be $+19.3 \pm 7.6$ (stat.) ± 2.6 (syst.) MeV/c in which the positive sign means the u quarks are correlated with the proton spin and proton momentum following the right-hand rule: $k_T^u \cdot (\vec{S} \times \vec{P}) > 0$. To the contrary, the average $\langle k_T^d \rangle$ is estimated to be $-40.2 \pm 23.0 \pm 9.3$ MeV/c, showing an opposite sign and a similar magnitude compared to $\langle k_T^u \rangle$. This is roughly con-

sistent with the u - d correlation in SIDIS measurements at a much lower scale (although Sivers function evolution effects may enter), observed as 96_{-28}^{+60} and -113_{-51}^{+45} MeV for u and d , respectively [19]. We also find that the gluon and sea quarks are consistent with zero within a 10.0 MeV/ c total uncertainty (the average $\langle k_T^{g+sea} \rangle = 5.2 \pm 9.3 \pm 3.8$ MeV/ c). These findings conserve the momentum sum rule and also help verify the inverted parton $\langle k_T \rangle$ results. Our measurement probes a range $0.03 < x < 0.6$ (u and d quarks), and $0.01 < x < 0.5$ (gluons); bin-by-bin parton x and $\langle k_T \rangle$ values are listed in the accompanying material [51].

In summary, transverse single-spin asymmetries for dijet production in pp collisions are measured in jet-charge bins using 200 GeV data at STAR. This is the first time that nonzero Sivers signals in pp -induced dijet production are observed. Through $\Delta(\zeta)$ -to- $\langle k_T \rangle$ conversion and pseudo-inversion, the $\langle k_T \rangle$ for individual partons are unfolded in a kinematic approach. The u - and d -quark $\langle k_T \rangle$ are found to have opposite signs and similar magnitudes, while $\langle k_T \rangle$ for gluon and sea quarks combined is consistent with zero. Analyses of larger data sets, both in hand and in progress, with extension to more forward rapidity, may enable more precise determination of Sivers partonic $\langle k_T \rangle$ values and potentially further elucidate their kinematic behavior. Inclusion of these data in future global analyses will enhance a consistent extraction of Sivers

observables and may also impact our understanding of evolution effects, process dependence and other important issues relating to the Sivers TMD function.

We thank the RHIC Operations Group and RCF at BNL, the NERSC Center at LBNL and the Open Science Grid consortium for providing resources and support. This work was supported in part by the Office of Nuclear Physics within the U.S. DOE Office of Science, the U.S. National Science Foundation, National Natural Science Foundation of China, Chinese Academy of Science, the Ministry of Science and Technology of China and the Chinese Ministry of Education, the Higher Education Sprout Project by Ministry of Education at NCKU, the National Research Foundation of Korea, Czech Science Foundation and Ministry of Education, Youth and Sports of the Czech Republic, Hungarian National Research, Development and Innovation Office, New National Excellency Programme of the Hungarian Ministry of Human Capacities, Department of Atomic Energy and Department of Science and Technology of the Government of India, the National Science Centre and WUT ID-UB of Poland, the Ministry of Science, Education and Sports of the Republic of Croatia, German Bundesministerium für Bildung, Wissenschaft, Forschung und Technologie (BMBF), Helmholtz Association, Ministry of Education, Culture, Sports, Science and Technology (MEXT) and Japan Society for the Promotion of Science (JSPS).

-
- [1] C. A. Aidala, S. D. Bass, D. Hasch, and G. K. Mallot, Rev. Mod. Phys. **85**, 655 (2013), arXiv:1209.2803 [hep-ph].
- [2] M. Anselmino, A. Mukherjee, and A. Vossen, Progress in Particle and Nuclear Physics **114**, 103806 (2020).
- [3] A. Accardi *et al.*, Eur. Phys. J. A **52**, 268 (2016), arXiv:1212.1701 [nucl-ex].
- [4] D. Sivers, Phys. Rev. D **41**, 83 (1990).
- [5] G. L. Kane, J. Pumplin, and W. Repko, Phys. Rev. Lett. **41**, 1689 (1978).
- [6] J. Adam *et al.* (STAR Collaboration), Phys. Rev. D **103**, 092009 (2021).
- [7] J. Qiu and G. Sterman, Phys. Rev. D **59**, 014004 (1998).
- [8] A. V. Efremov and O. V. Teryaev, Sov. J. Nucl. Phys. **36**, 140 (1982).
- [9] D. Boer, P. Mulders, and F. Pijlman, Nuclear Physics B **667**, 201 (2003).
- [10] A. Airapetian *et al.* (The HERMES Collaboration), Phys. Rev. Lett. **94**, 012002 (2005).
- [11] A. Airapetian *et al.*, Phys. Rev. Lett. **103**, 152002 (2009).
- [12] X. Qian *et al.*, Phys. Rev. Lett. **107**, 072003 (2011).
- [13] C. Adolph *et al.*, Phys. Lett. B **717**, 383 (2012).
- [14] K. Allada *et al.* (Jefferson Lab Hall A Collaboration), Phys. Rev. C **89**, 042201 (2014).
- [15] C. Adolph *et al.*, Physics Letters B **744**, 250 (2015).
- [16] M. Anselmino, M. Boglione, U. D'Alesio, A. Kotzinian, F. Murgia, and A. Prokudin, Phys. Rev. D **72**, 094007 (2005).
- [17] W. Vogelsang and F. Yuan, Phys. Rev. D **72**, 054028 (2005).
- [18] J. C. Collins, A. V. Efremov, K. Goeke, S. Menzel, A. Metz, and P. Schweitzer, Phys. Rev. D **73**, 014021 (2006).
- [19] M. Anselmino, M. Boglione, U. D'Alesio, A. Kotzinian, S. Melis, F. Murgia, A. Prokudin, and C. Türk, The European Physical Journal A **39**, 89 (2008).
- [20] A. Bacchetta and M. Radici, Phys. Rev. Lett. **107**, 212001 (2011).
- [21] P. Sun and F. Yuan, Phys. Rev. D **88**, 114012 (2013).
- [22] M. G. Echevarria, A. Idilbi, Z.-B. Kang, and I. Vitev, Phys. Rev. D **89**, 074013 (2014).
- [23] M. Anselmino, M. Boglione, U. D'Alesio, F. Murgia, and A. Prokudin, J. High Energy Phys. **2017** (4), 46.
- [24] M. Boglione, U. D'Alesio, C. Flore, J. Gonzalez-Hernandez, F. Murgia, and A. Prokudin, Physics Letters B **815**, 136135 (2021).
- [25] A. Bacchetta, F. Delcarro, C. Pisano, and M. Radici, Physics Letters B **827**, 136961 (2022).
- [26] M. Burkardt, Phys. Rev. D **69**, 091501(R) (2004).
- [27] A. Bacchetta *et al.* (MAP Collaboration), J. High Energy Phys. **2022** (10), 127.
- [28] J. Cammarota, L. Gamberg, Z.-B. Kang, J. A. Miller, D. Pitonyak, A. Prokudin, T. C. Rogers, and N. Sato (Jefferson Lab Angular Momentum (JAM) Collaboration), Phys. Rev. D **102**, 054002 (2020).
- [29] M. Bury, A. Prokudin, and A. Vladimirov, Phys. Rev. Lett. **126**, 112002 (2021).
- [30] M. G. Echevarria, Z.-B. Kang, and J. Terry, Journal of High Energy Physics **2021**, 10.1007/jhep01(2021)126 (2021).

- [31] S. J. Brodsky, D. S. Hwang, and I. Schmidt, *Physics Letters B* **530**, 99 (2002).
- [32] J. C. Collins, *Phys. Lett. B* **536**, 43 (2002), arXiv:hep-ph/0204004 [hep-ph].
- [33] M. Grosse Perdekamp and F. Yuan, *Annual Review of Nuclear and Particle Science* **65**, 429 (2015), <https://doi.org/10.1146/annurev-nucl-102014-021948>.
- [34] M. Aghasyan *et al.*, *Phys. Rev. Lett.* **119**, 112002 (2017), arXiv:1704.00488 [hep-ex].
- [35] L. Adamczyk *et al.*, *Phys. Rev. Lett.* **116**, 132301 (2016).
- [36] D. Boer and W. Vogelsang, *Phys. Rev. D* **69**, 094025 (2004), arXiv:hep-ph/0312320 [hep-ph].
- [37] D. Boer, C. Lorcé, C. Pisano, and J. Zhou, *Adv. High Energy Phys.* **2015**, 371396 (2015), arXiv:1504.04332 [hep-ph].
- [38] C. J. Bomhof and P. J. Mulders, *AIP Conference Proceedings* **915**, 563 (2007), <https://aip.scitation.org/doi/pdf/10.1063/1.2750844>.
- [39] B. I. Abelev *et al.*, *Phys. Rev. Lett.* **99**, 142003 (2007).
- [40] A. Bacchetta, C. J. Bomhof, P. J. Mulders, and F. Pijlman, *Phys. Rev. D* **72**, 034030 (2005).
- [41] T. C. Rogers and P. J. Mulders, *Phys. Rev. D* **81**, 094006 (2010).
- [42] X. Liu, F. Ringer, W. Vogelsang, and F. Yuan, *Phys. Rev. D* **102**, 114012 (2020).
- [43] Z.-B. Kang, K. Lee, D. Y. Shao, and J. Terry, *Journal of High Energy Physics* **2021**, 66 (2021), arXiv:2008.05470 [hep-ph].
- [44] K. H. Ackermann *et al.*, *Nucl. Instrum. Methods Phys. Res., Sect. A* **499**, 624 (2003).
- [45] M. Anderson *et al.*, *Nucl. Instrum. Methods Phys. Res., Sect. A* **499**, 659 (2003).
- [46] M. Beddo *et al.*, *Nucl. Instrum. Methods Phys. Res., Sect. A* **499**, 725 (2003).
- [47] C. Allgower *et al.*, *Nucl. Instrum. Methods Phys. Res., Sect. A* **499**, 740 (2003).
- [48] RHIC Polarimetry Group, *RHIC/CAD Accelerator Physics Note*, 490 (2013).
- [49] M. Cacciari, G. P. Salam, and G. Soyez, *JHEP* **04**, 063.
- [50] J. Adam *et al.*, *Phys. Rev. D* **98**, 032011 (2018).
- [51] See supplementary material at [URL will be inserted by publisher].
- [52] P. Z. Skands, *Phys. Rev. D* **82**, 074018 (2010).
- [53] T. Sjostrand, S. Mrenna, and P. Z. Skands, *JHEP* **05**, 026.
- [54] P. Z. Skands, (2014), arXiv:1005.3457v5 [hep-ph].
- [55] GEANT Detector description and simulation tool, CERN Program Library Long Write-up W5013, CERN Geneva.
- [56] D. Krohn, M. D. Schwartz, T. Lin, and W. J. Waalewijn, *Phys. Rev. Lett.* **110**, 212001 (2013).

Supplemental Material to: Measurement of transverse single-spin asymmetries for dijet production in polarized proton-proton collisions at $\sqrt{s} = 200$ GeV

(STAR Collaboration)
(Dated: February 6, 2024)

I. 3-GAUSSIAN FIT

An example of a 3-Gaussian fit ($N(\zeta) = p_0 \cdot (e^{-\frac{(\zeta-p_1)^2}{2p_2^2}} + p_3 \cdot e^{-\frac{(\zeta-p_4)^2}{2p_4^2}} + p_5 \cdot e^{-\frac{(\zeta-p_6)^2}{2p_6^2}})$) of the $N(\zeta)$ distribution for ζ within $\phi_b \in [15^\circ, 30^\circ]$ and $\eta^{total} \in [0, 0.8]$ using unpolarized +tagged +z beam data is shown in Fig. 1.

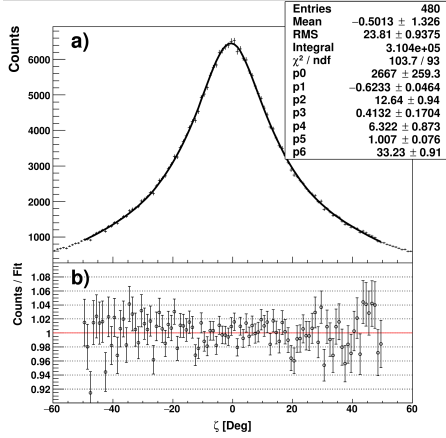


FIG. 1. Distribution of ζ in the range of $\phi_b \in [15^\circ, 30^\circ]$ and $\eta^{total} \in [0, 0.8]$ of the unpolarized +tagging data for the +z beam. A 3-Gaussian fit is performed within the range $\pm 50^\circ$. The lower panel shows a ratio of counts over the fit.

The triple Gaussian shape is chosen for the ζ fitting because it captures the salient features of the ζ distribution. The distribution itself is driven by broad (Gaussian) widths arising largely from multi-GeV intrinsic ("primordial") k_T and initial-state radiation (ISR) effects, in convolution with various responses arising from the STAR detector readout and triggering. Features may be further shaped by the influence of jet-patch triggering thresholds, supplying events with different average p_T . However, there is no detailed accounting of contributing magnitudes, nor the relevance or role played by several of the possible modifications. Hence it is most important to note, that our extracted dijet Siverts effect results are largely insensitive to variations of the empirically-driven function shape choice.

II. COSINE FIT

An example of a cosine fit ($\Delta\langle\zeta\rangle(\phi_b) = p_0 \cdot \cos(\phi_b)$) for $\Delta\langle\zeta\rangle$ -vs- ϕ_b in the range of $\eta^{total} \in [0, 0.8]$ is shown in Fig. 2. In the toy model, a constant 5 MeV/c $\langle k_T \rangle$ is separately inserted in the corrected data along the +x and -x directions to mimic a Siverts effect in the spin-up and spin-down states, respectively.

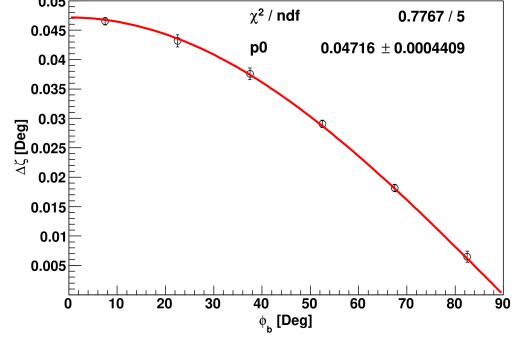


FIG. 2. Example of a Cosine fit with $\langle k_T \rangle = 5$ MeV/c manually inserted in corrected data for $\eta^{total} \in [0, 0.8]$.

III. PARTON FRACTIONS

The overall Siverts dijet effect comes from four contributions: u , d , gluons, and sea quarks. In our analysis, since the sea quark fraction is relatively low and their overall contribution is expected to be small, its contribution is combined with that of the gluons. Along with the four charge tagged $\langle k_T \rangle$ results, there are then enough constraints to solve for the $\langle k_T \rangle$ of the three parton sources.

A requirement for obtaining the solutions is the parton fractions in each charge tagged bin, which can be estimated from the embedding. Table I shows the parton fractions after combining all the data sets (JP and run), as well as combining results from both the +z going (Blue) and -z going (Yellow) beams. The u quark fraction sequentially decreases from the plus-tagging to 0^+ , 0^- , and the minus-tagging, while the d quark fraction increases. The quark fraction, particularly the u quark fraction, is positively correlated with η^{tot} , which is proportional to $\log(x_1/x_2)$. To the contrary, the gluon fraction has a negative correlation with η^{tot} . Because of the statistical uncertainties associated with the inversion, these effects are not strongly manifest in our results for partonic $\langle k_T \rangle$.

IV. INDIVIDUAL PARTON $\langle k_T \rangle$ RESULTS

The numerical values, including the statistical and systematic errors, for the bin-by-bin parton $\langle k_T \rangle$ values are listed in Table II.

$+$ $_{tag}$	$\langle \eta^{tot} \rangle$	[-3.6, -2.6]	[-2.6, -1.6]	[-1.6, -0.8]	[-0.8, 0]
	f^u	$0.047^{+0.046}_{-0.029}$	$0.154^{+0.032}_{-0.031}$	$0.239^{+0.040}_{-0.040}$	$0.313^{+0.045}_{-0.045}$
	f^d	$0.175^{+0.072}_{-0.061}$	$0.061^{+0.015}_{-0.014}$	$0.077^{+0.013}_{-0.013}$	$0.086^{+0.013}_{-0.013}$
	f^{g+sea}	$0.778^{+0.139}_{-0.100}$	$0.785^{+0.045}_{-0.044}$	$0.684^{+0.041}_{-0.041}$	$0.601^{+0.045}_{-0.045}$
	$\langle \eta^{tot} \rangle$	[0, 0.8]	[0.8, 1.6]	[1.6, 2.6]	[2.6, 3.6]
	f^u	$0.433^{+0.044}_{-0.044}$	$0.578^{+0.049}_{-0.049}$	$0.670^{+0.048}_{-0.048}$	$0.798^{+0.082}_{-0.097}$
	f^d	$0.109^{+0.014}_{-0.014}$	$0.112^{+0.015}_{-0.015}$	$0.128^{+0.021}_{-0.020}$	$0.175^{+0.088}_{-0.071}$
f^{g+sea}	$0.458^{+0.038}_{-0.038}$	$0.311^{+0.036}_{-0.035}$	$0.202^{+0.039}_{-0.038}$	$0.027^{+0.152}_{-0.019}$	
$-$ $_{tag}$	$\langle \eta^{tot} \rangle$	[-3.6, -2.6]	[-2.6, -1.6]	[-1.6, -0.8]	[-0.8, 0]
	f^u	$0.048^{+0.039}_{-0.026}$	$0.060^{+0.015}_{-0.014}$	$0.089^{+0.016}_{-0.016}$	$0.141^{+0.024}_{-0.024}$
	f^d	$0.061^{+0.042}_{-0.030}$	$0.107^{+0.025}_{-0.024}$	$0.161^{+0.026}_{-0.026}$	$0.178^{+0.025}_{-0.025}$
	f^{g+sea}	$0.891^{+0.100}_{-0.075}$	$0.833^{+0.040}_{-0.038}$	$0.750^{+0.034}_{-0.034}$	$0.681^{+0.037}_{-0.036}$
	$\langle \eta^{tot} \rangle$	[0, 0.8]	[0.8, 1.6]	[1.6, 2.6]	[2.6, 3.6]
	f^u	$0.200^{+0.030}_{-0.030}$	$0.272^{+0.038}_{-0.038}$	$0.406^{+0.062}_{-0.061}$	$0.466^{+0.137}_{-0.134}$
	f^d	$0.258^{+0.034}_{-0.034}$	$0.268^{+0.035}_{-0.035}$	$0.350^{+0.065}_{-0.064}$	$0.170^{+0.117}_{-0.086}$
f^{g+sea}	$0.542^{+0.039}_{-0.039}$	$0.461^{+0.048}_{-0.047}$	$0.244^{+0.069}_{-0.055}$	$0.364^{+0.290}_{-0.145}$	
0^+ $_{tag}$	$\langle \eta^{tot} \rangle$	[-3.6, -2.6]	[-2.6, -1.6]	[-1.6, -0.8]	[-0.8, 0]
	f^u	$0.151^{+0.063}_{-0.055}$	$0.110^{+0.028}_{-0.027}$	$0.191^{+0.035}_{-0.035}$	$0.239^{+0.033}_{-0.033}$
	f^d	$0.031^{+0.034}_{-0.021}$	$0.079^{+0.021}_{-0.020}$	$0.101^{+0.019}_{-0.019}$	$0.132^{+0.019}_{-0.019}$
	f^{g+sea}	$0.818^{+0.106}_{-0.080}$	$0.811^{+0.047}_{-0.044}$	$0.708^{+0.039}_{-0.039}$	$0.629^{+0.036}_{-0.036}$
	$\langle \eta^{tot} \rangle$	[0, 0.8]	[0.8, 1.6]	[1.6, 2.6]	[2.6, 3.6]
	f^u	$0.360^{+0.043}_{-0.043}$	$0.448^{+0.046}_{-0.046}$	$0.612^{+0.049}_{-0.049}$	$0.663^{+0.062}_{-0.063}$
	f^d	$0.152^{+0.021}_{-0.020}$	$0.177^{+0.027}_{-0.027}$	$0.179^{+0.026}_{-0.026}$	$0.194^{+0.046}_{-0.044}$
f^{g+sea}	$0.487^{+0.038}_{-0.038}$	$0.375^{+0.042}_{-0.042}$	$0.209^{+0.037}_{-0.036}$	$0.144^{+0.052}_{-0.042}$	
0^- $_{tag}$	$\langle \eta^{tot} \rangle$	[-3.6, -2.6]	[-2.6, -1.6]	[-1.6, -0.8]	[-0.8, 0]
	f^u	$0.036^{+0.029}_{-0.020}$	$0.082^{+0.022}_{-0.020}$	$0.117^{+0.023}_{-0.022}$	$0.201^{+0.028}_{-0.028}$
	f^d	$0.109^{+0.049}_{-0.042}$	$0.079^{+0.020}_{-0.018}$	$0.133^{+0.025}_{-0.024}$	$0.153^{+0.022}_{-0.022}$
	f^{g+sea}	$0.855^{+0.087}_{-0.070}$	$0.838^{+0.045}_{-0.043}$	$0.750^{+0.041}_{-0.041}$	$0.646^{+0.037}_{-0.037}$
	$\langle \eta^{tot} \rangle$	[0, 0.8]	[0.8, 1.6]	[1.6, 2.6]	[2.6, 3.6]
	f^u	$0.279^{+0.034}_{-0.034}$	$0.373^{+0.039}_{-0.039}$	$0.530^{+0.046}_{-0.046}$	$0.659^{+0.078}_{-0.081}$
	f^d	$0.198^{+0.026}_{-0.026}$	$0.217^{+0.033}_{-0.033}$	$0.211^{+0.033}_{-0.033}$	$0.214^{+0.067}_{-0.061}$
f^{g+sea}	$0.523^{+0.040}_{-0.040}$	$0.410^{+0.046}_{-0.046}$	$0.259^{+0.047}_{-0.046}$	$0.127^{+0.084}_{-0.047}$	

TABLE I. Parton fraction and statistical uncertainty after Blue and Yellow beam combination for individual partons in the four tagged bins. The JP2 and JP1 triggers in the 2012 embedding and the 2015 embedding are all combined together.

V. SYSTEMATIC UNCERTAINTIES

The total systematic uncertainty and each individual contribution for the bin-by-bin and average parton $\langle k_T \rangle$ values are listed in Table III.

The average parton $\langle x \rangle$ and $\langle k_T \rangle$ [MeV/c]					
η^{total}	[-3.6, -1.6]	[-1.6, 0]	[0, 1.6]	[1.6, 3.6]	
$\langle x^u \rangle$	0.05 ± 0.02	0.11 ± 0.05	0.22 ± 0.09	0.36 ± 0.11	
$\langle k_T^u \rangle$ [MeV/c]	-36.4 ± 139.4	11.2 ± 20.3	20.0 ± 9.7	26.6 ± 21.8	
$\langle x^d \rangle$	0.04 ± 0.02	0.11 ± 0.05	0.20 ± 0.08	0.33 ± 0.09	
$\langle k_T^d \rangle$ [MeV/c]	-46.5 ± 247.9	-92.7 ± 53.7	-34.1 ± 31.9	9.8 ± 63.7	
$\langle x^{g+sea} \rangle$	0.04 ± 0.02	0.09 ± 0.04	0.17 ± 0.07	0.30 ± 0.09	
$\langle k_T^{g+sea} \rangle$ [MeV/c]	10.8 ± 38.9	10.6 ± 13.8	-0.2 ± 16.2	-83.2 ± 89.5	

TABLE II. The average x and inverted parton $\langle k_T \rangle$ for u , d , and $g+sea$ in each η^{total} region. The rms of x and the total uncertainty of $\langle k_T \rangle$ are also given in the table.

Systematic uncertainties of parton $\langle k_T \rangle$ [MeV/c]						
	η^{total}	[-3.6, -1.6]	[-1.6, 0]	[0, 1.6]	[1.6, 3.6]	Avg
u	Simulation	53.5	6.5	2.6	8.0	2.3
	Fitting	15.8	2.4	1.1	5.9	1.0
	Measurement	4.4	1.1	0.9	0.8	0.5
	Total	55.9	7.0	3.0	10.0	2.6
d	Simulation	85.7	23.6	9.8	28.5	8.6
	Fitting	29.2	6.1	3.8	15.5	3.2
	Measurement	14.0	2.9	1.5	2.2	1.1
	Total	91.6	24.6	10.6	32.6	9.3
$g+sea$	Simulation	14.3	5.6	4.9	40.2	3.6
	Fitting	4.5	1.6	1.9	22.0	1.2
	Measurement	1.9	0.6	0.9	3.5	0.5
	Total	15.1	5.8	5.4	46.0	3.8

TABLE III. The total systematic uncertainty [MeV/c] of each parton $\langle k_T \rangle$ and breakdown of individual contributions for each η^{total} region and the average of all η^{total} regions.

ACKNOWLEDGEMENTS

We thank the RHIC Operations Group and RCF at BNL, the NERSC Center at LBNL and the Open Science Grid consortium for providing resources and support. This work was supported in part by the Office of Nuclear Physics within the U.S. DOE Office of Science, the U.S. National Science Foundation, National Natural Science Foundation of China, Chinese Academy of Science, the Ministry of Science and Technology of China and the Chinese Ministry of Education, the Higher Education Sprout Project by Ministry of Education at NCKU, the National Research Foundation of Korea, Czech Science Foundation and Ministry of Education, Youth and Sports of the Czech Republic, Hungarian National Research, Development and Innovation Office, New National Excellency Programme of the Hungarian Ministry of Human Capacities, Department of Atomic Energy and Department of Science and Technology of the Government of India, the National Science Centre and WUT ID-UB of Poland, the Ministry of Science, Education and Sports of the Republic of Croatia, German Bundesministerium für Bildung, Wissenschaft, Forschung and Technologie (BMBF), Helmholtz Association, Ministry of Education,

Culture, Sports, Science and Technology (MEXT) and Japan Society for the Promotion of Science (JSPS).